

## Log-elastographic and non-marching full inversion schemes for shear modulus recovery from single frequency elastographic data

This article has been downloaded from IOPscience. Please scroll down to see the full text article.

2009 Inverse Problems 25 075004

(<http://iopscience.iop.org/0266-5611/25/7/075004>)

[The Table of Contents](#) and [more related content](#) is available

Download details:

IP Address: 128.113.82.223

The article was downloaded on 16/09/2009 at 14:45

Please note that [terms and conditions apply](#).

# Log-elastographic and non-marching full inversion schemes for shear modulus recovery from single frequency elastographic data

Kui Lin, Joyce McLaughlin and Ning Zhang

Mathematics Department, Rensselaer Polytechnic Institute, 110 8th Street, Troy, NY 12180, USA

E-mail: [link@rpi.edu](mailto:link@rpi.edu), [mclauj@rpi.edu](mailto:mclauj@rpi.edu) and [zhangn@rpi.edu](mailto:zhangn@rpi.edu)

Received 6 September 2008, in final form 17 March 2009

Published 26 May 2009

Online at [stacks.iop.org/IP/25/075004](http://stacks.iop.org/IP/25/075004)

## Abstract

The goal of elastography is to image the shear stiffness of tissue for cancer diagnosis and the focus of this paper is on single frequency elastographic data. Assuming that the measured displacement of the propagating shear wave satisfies the acoustic wave equation, the shear modulus  $\mu$  can be recovered by solving a first-order partial differential equation in the inverse problem. To capture possible exponential growth and decay of the targeted parameter  $\mu$  numerically in a stable manner, we propose a log-elastographic nonlinear scheme and a linear finite difference based elliptic scheme. Both methods are shown to be convergent at first order and their performances are compared with the performances of a semi-implicit upwind scheme and the direct inversion model previously investigated (see [23]). We present shear modulus reconstructions from synthetic data with and without noise.

(Some figures in this article are in colour only in the electronic version)

## 1. Introduction

In this paper, we investigate the stability and accuracy of several finite difference based numerical schemes that are developed to solve the first-order partial differential equation involved in the full inversion model, see [23], in the inverse problem of elastography. The target application of elastography is the successful imaging of shear stiffness in tissue and the goal is to develop a new medical tool for cancer diagnosis. All experiments involve mechanically displacing the tissue, which is achieved by either static compression, harmonic oscillation or transient pulses. The interior displacement tissue response is measured on a fine grid by either ultrasound [2–8, 10, 14, 16, 17, 19–21, 30, 31, 33, 34, 40–42] or magnetic resonance imaging [15, 24–26, 29, 32, 35–38].

The focus of this paper is on single frequency displacement data, which can be measured in the dynamic excitation experiments and the transient experiments. In the dynamic experiments, a time harmonic excitation is made on the boundary or in the interior to create a time harmonic wave. In the transient experiments, the tissue is initially at rest and a broadband pulse with central frequency 50 Hz–200 Hz is applied either on the boundary or along a line in the interior and excites displacement in the media. From the mechanical response to the excitation, an inverse problem needs to be solved to determine the shear modulus. Many of the inversion approaches proposed so far reduce the linear elastic equation system to the Helmholtz equation for a single displacement component. Furthermore, they invoke the locally constant assumption and recover the elastic parameter by simple algebraic inversion (see [2, 3, 9, 11, 14, 24–26, 29, 30, 32]). Finite element based methods have also been developed to handle the complete equations of elasto-dynamics with 3D displacement field by either an optimization approach (see [35–38]) or direct solving (see [27]). In this work, however, we develop finite difference based numerical methods to reconstruct the shear modulus from single component displacement data. The locally constant assumption is avoided and the inverse problem is solved by solving a first-order PDE.

Based on the discussions of the experiments given in [23], we assume the forward problem for the single component measured displacement is governed by the following wave equation:

$$\nabla \cdot (\mu(x, y) \nabla u(x, y, t)) = \rho(x, y) u_{tt}(x, y, t) \quad \text{in } \Omega \times (0, T), \quad (1)$$

where the domain  $\Omega \in \mathbb{R}^2$ , the density  $\rho \in \mathbb{C}^1(\bar{\Omega})$  and the shear modulus  $\mu \in \mathbb{C}^2(\bar{\Omega})$  are assumed to be real. Consistent with the experiment, either a single frequency continuous excitation on the boundary or a broadband pulse with a central frequency is assumed:

$$u(x, y, 0) = u_t(x, y, 0) = 0 \quad \text{on } \Omega, \quad (2)$$

$$\mu(x, y) \nabla u(x, y, t) \cdot \nu(x, y) = g(x, y, t) \quad \text{on } \partial\Omega \times (0, T). \quad (3)$$

In this paper, we use  $g(x, y)$  as the boundary excitation in the simulation while the boundary condition above can also be replaced by

$$u(x, y, t) = f(x, y, t) \quad \text{on } \partial\Omega \times (0, T). \quad (4)$$

For the inverse problem model, we first change the targeted parameter in the inverse problem to be the ratio between the modulus and density  $\tilde{\mu} = \mu/\rho$  by making the commonly accepted assumption that  $\rho(x, y)$  is a constant.

$$\begin{aligned} \nabla \cdot (\mu(x, y) \nabla u(x, y, t)) &= \rho(x, y) u_{tt}(x, y, t), \\ \tilde{\mu} = \frac{\mu}{\rho} \Rightarrow \nabla \cdot (\tilde{\mu}(x, y) \nabla u(x, y, t)) &= u_{tt}(x, y, t). \end{aligned}$$

Then we extract the central or main frequency content of the measured data by Fourier transforming the equation to the frequency domain. Denoting  $\omega_c$  as the central or main frequency, we get

$$\left. \begin{aligned} \nabla \cdot (\tilde{\mu}(x, y) \nabla u(x, y, t)) &= u_{tt}(x, y, t) \\ \hat{u}(x, y, \omega) &= \frac{1}{\sqrt{2\pi}} \int_{-\infty}^{+\infty} e^{-i\omega t} u(x, y, t) dt \end{aligned} \right\} \implies \quad (5)$$

$$\begin{aligned} \nabla \cdot (\tilde{\mu}(x, y) \nabla \hat{u}(x, y, \omega_c)) &= -\omega_c^2 \hat{u}(x, y, \omega_c) \implies \\ \nabla \tilde{\mu}(x, y) \cdot \nabla \hat{u}(x, y, \omega_c) + \tilde{\mu}(x, y) \Delta \hat{u}(x, y, \omega_c) + \omega_c^2 \hat{u}(x, y, \omega_c) &= 0. \end{aligned}$$

As a widely accepted practice in the inverse problem of elastography, a simple algebraic inversion model, called the direct inversion model, can be achieved by making the locally

constant assumption on  $\mu$  and neglecting the first derivative terms of  $\tilde{\mu}$  from (5):

$$\hat{\mu}(x, y)\Delta\hat{u}(x, y, \omega_c) + \omega_c^2\hat{u}(x, y, \omega_c) = 0, \quad (6)$$

where we denote the approximated  $\tilde{\mu}$  by  $\hat{\mu}$ .

Under some hypotheses,  $\hat{\mu}$  is a good approximation to  $\tilde{\mu}$ ; see [23] for a rigorously established bound on the relative difference. However, when there are a number of high contrast inclusions, solving the first-order PDE. Equation (5) can yield a more reliable image. This paper then is to consider reconstruction of  $\tilde{\mu}$  by the full inversion model: that is, find  $\tilde{\mu}$  by solving

$$\nabla\tilde{\mu}(x, y) \cdot \nabla\hat{u}(x, y, \omega_c) + \tilde{\mu}(x, y)\Delta\hat{u}(x, y, \omega_c) + \omega_c^2\hat{u}(x, y, \omega_c) = 0. \quad (7)$$

To recover  $\tilde{\mu}$  from the full inversion equation (7), we have to

- establish real differential equation models from the complex equation model (7) as our target  $\tilde{\mu}$  is a real quantity;
- develop robust schemes to solve the first-order partial differential equation with variable coefficients.

The first task can be accomplished by a variety of procedures while the second one requires a lot more attention. There have been a lot of methods proposed for computing the numerical solutions of first-order PDEs, they are mainly designed to handle forward simulations so they have major limitations in our inverse problem of wave propagation. One of the difficulties lies in the fact that the exact solution of equation (7) could have rapid exponential growth and decay, which is hard to capture by most of the schemes developed so far. Another difficulty is that our equation does not have a specific time direction and the information flows are so complicated that simply following the characteristics is not a successful approach. In [13], Fattal and Kupferman introduced the concept of logarithmic variables in the simulation of viscoelastic flows. Their log-conformation representation of the constitutive laws removes the instability from the numerical solution and enables a weak stability constraint on the spatial step size. In this work, we adapt their concept and develop a log-elastographic nonlinear finite difference based numerical scheme to reconstruct  $\tilde{\mu}$  by solving the inverse problem model as a evolution type of PDE. In addition to removing numerical instability, the proposed nonlinear scheme captures the exponential growth and decay of the exact solution successfully. We present a first-order upwind version of the method and the corresponding stability and accuracy result. We also develop another finite difference based elliptic scheme for the full inversion, where the basic concept is to solve the differential equation as a strictly diagonally dominant linear system. We prove that the elliptic scheme is convergent of first order. Compared with a semi-implicit upwind scheme and the direct inversion local scheme, the log-elastographic nonlinear scheme and the linear elliptic scheme are more stable and reliable to recover rapidly changing shear moduli in the inverse problem. The PDE solvers also exhibit more robustness with respect to noise than the direct inversion method.

The structure of this paper is as follows: in section 2, we present two ways to extract the real part of the full inversion (7). Then we give the stability and accuracy of a standard semi-implicit upwind scheme in section 3. The upwind nonlinear scheme is presented and analyzed in section 4 while the construction and the convergence result of the linear elliptic scheme is given in section 5. Section 6 is devoted to the exhibition of numerical reconstructions. Finally, we conclude this document and give ideas on future work.

## 2. Real equation models for full inversion

To transfer (7) to a real equation, we first propose to solve the inverse problem as a evolution type of differential equation. Assuming that the wave propagates in the  $x$ -direction in the

forward problem and  $|\hat{u}_x| \neq 0$ , we divide both sides of (7) by  $\hat{u}_x$  and take the real part of the resulting equation, which gives us the following model:

$$\tilde{\mu}_x + a(x, y)\tilde{\mu}_y + b(x, y)\tilde{\mu} + c(x, y) = 0, \quad (8)$$

where

$$a(x, y) = \text{real}\left(\frac{\hat{u}_y}{\hat{u}_x}\right), \quad b(x, y) = \text{real}\left(\frac{\Delta\hat{u}}{\hat{u}_x}\right), \quad c(x, y) = \text{real}\left(\frac{\omega_c^2\hat{u}}{\hat{u}_x}\right).$$

We take the real part of equation (7) in this way because our experience with our specific application shows that the amplitude of the resultant  $a(x, y)$  is usually well controlled. We treat  $x$  as a pseudo time direction and the inverse problem solution is calculated as the solution of a transport equation. In this case, the information of the target value  $\tilde{\mu}$  is only allowed to ‘flow’ into the domain from one portion of the boundary and the solution is unique. The control of  $a(x, y)$  makes the corresponding CFL condition easy to satisfy with additional interpolation of the displacement data. Our first two methods, the semi-implicit upwind scheme and the log-elastographic nonlinear scheme are designed to handle equation (8). For both of these methods, we will require initial data at the starting ‘time’ where here that is at  $x = 0$ . Our choice is given by *a priori* information or by a direct inversion estimate (see [23]). For side conditions, we use the Neumann boundary condition.

For our third method, equation (7) is treated differently. We separate the phase and amplitude of the complex data  $\hat{u} = Me^{i\phi}$ , rewrite all the derivatives of  $\hat{u}$  in terms of  $M$  and  $\phi$ , eliminate the common factor  $e^{i\phi}$  from both sides of the equation and take the real part of the resulting equation as the inverse problem model:

$$\begin{aligned} \nabla\tilde{\mu} \cdot \nabla\hat{u} + \tilde{\mu}\Delta\hat{u} + \omega_c^2\hat{u} &= 0, \quad \hat{u} = Me^{i\phi} \Rightarrow \\ \{(M_x + iM\phi_x)\tilde{\mu}_x + (M_y + iM\phi_y)\tilde{\mu}_y + [\Delta M - |\nabla\phi|^2 M \\ + i(2\nabla M\nabla\phi + M\Delta\phi)]\tilde{\mu} + \omega_c^2 M\}e^{i\phi} &= 0 \Rightarrow \\ M_x\tilde{\mu}_x + M_y\tilde{\mu}_y + \tilde{\mu}(\Delta M - |\nabla\phi|^2 M) + \omega_c^2 M &= 0. \end{aligned} \quad (9)$$

The reasoning behind this treatment is that we want to preserve the non-oscillatory features of equation (7). For equation (9), we develop a completely different scheme for computing  $\tilde{\mu}$ ; this method has more in common with elliptic schemes than hyperbolic schemes. Here we require Dirichlet boundary condition on all sides of our domain where again this is determined by *a priori* information or direct inversion estimate (see [23]). To establish the uniqueness of the solution  $\tilde{\mu}$  in this set up, we require that  $|\hat{u}_x| \neq 0$  and refer to [18, 28] for the proof of uniqueness in an elliptic inverse problem. The derivation of (8) and the uniqueness of the solution of (9) rely on the assumption that  $|\hat{u}_x| \neq 0$ , which will be investigated in future work.

For all the numerical schemes and reconstruction examples presented in this paper, we use a two-dimensional square domain  $[0, L] \times [-L/2, L/2]$ . We let  $dx_i$  denote the pseudo time step size at the  $i$ th step and  $dy$  denote the transverse spatial step size in the inverse problem model (8). For (9), however,  $dx$  and  $dy$  will be used for spatial step sizes.

### 3. Linear semi-implicit upwind scheme

First, we give the stability and accuracy result of a semi-implicit upwind scheme that is designed to solve (8). For the detailed proof of the results in this section, see [22]. Consider the homogeneous part of (8):

$$\tilde{\mu}_x + a(x, y)\tilde{\mu}_y + b(x, y)\tilde{\mu} = 0. \quad (10)$$

If we use an upwind finite difference formulation to discretize  $\tilde{\mu}_y$  and make  $\tilde{\mu}$  implicit, we will have

$$\begin{aligned}
 & \left. \begin{aligned}
 a_{i,j} \geq 0 : & \frac{\tilde{\mu}_{i+1,j} - \tilde{\mu}_{i,j}}{dx_i} + a_{i,j} \frac{\tilde{\mu}_{i,j} - \tilde{\mu}_{i,j-1}}{dy} + b_{i,j} \tilde{\mu}_{i+1,j} = 0 \\
 a_{i,j} < 0 : & \frac{\tilde{\mu}_{i+1,j} - \tilde{\mu}_{i,j}}{dx_i} + a_{i,j} \frac{\tilde{\mu}_{i,j+1} - \tilde{\mu}_{i,j}}{dy} + b_{i,j} \tilde{\mu}_{i+1,j} = 0
 \end{aligned} \right\} \implies \\
 & a_{i,j} \geq 0 : \quad \tilde{\mu}_{i+1,j} = \frac{(1 - a_{i,j} \frac{dx_i}{dy}) \tilde{\mu}_{i,j} + a_{i,j} \frac{dx_i}{dy} \tilde{\mu}_{i,j-1}}{1 + b_{i,j} dx_i} \\
 & a_{i,j} < 0 : \quad \tilde{\mu}_{i+1,j} = \frac{(1 + a_{i,j} \frac{dx_i}{dy}) \tilde{\mu}_{i,j} - a_{i,j} \frac{dx_i}{dy} \tilde{\mu}_{i,j+1}}{1 + b_{i,j} dx_i} \\
 & 0 \leq i \leq m - 1, \quad 1 \leq j \leq n - 1, \quad n dy = L, \quad \sum_{i=1}^m dx_i = L,
 \end{aligned} \tag{11}$$

where  $\tilde{\mu}_{i,j}$  is the numerical solution for the finite difference operator. For the initial condition, we first assume that we are given *a priori*, the exact value for  $\tilde{\mu}_{i,j}$  at  $i = 0$  while on the boundaries, we use Neumann condition such that  $\tilde{\mu}_{i,0} = \tilde{\mu}_{i,2}$  and  $\tilde{\mu}_{i,n} = \tilde{\mu}_{i,n-2}$ .

**Lemma 1.** Suppose  $dx_i$  is small enough such that  $|a_{i,j}| dx_i / dy \leq 1$  and  $|b_{i,j}| dx_i < 1$ , then  $\exists \alpha$  independent of step sizes such that

$$\|\tilde{\mu}_{i+1}\|_\infty \leq e^{\alpha dx_i} \|\tilde{\mu}_i\|_\infty, \tag{12}$$

where  $\max_{i,j} \frac{1}{1+b_{i,j} dx_i} \leq e^{\alpha dx_i}$ .

The accuracy of the semi-implicit upwind discretization of (8) can now be proved by taking into account the stability result.

**Theorem 1.** Suppose all assumptions from lemma 1 are satisfied and  $\tilde{\mu}_{i,j}$  is the exact solution of (8) at node  $(i, j)$ . If the initial condition is exact, then  $\exists \hat{\alpha} > 0$  such that

$$|\tilde{\mu}_{i,j} - \tilde{\mu}_{i,j}| \leq \hat{\alpha} (dx + dy),$$

where  $dx = \max_i dx_i$ ,  $\hat{\alpha} = C^* e^{\alpha L} L$  and

$$C^* = \max_{0 \leq i \leq m} \left[ \max_{0 \leq j \leq n} \left( \frac{1}{2} \max(|\tilde{\mu}_{xx}(\xi_i, y_j)|, |\tilde{\mu}_{yy}(x_i, \eta_j)|) \right) \right]$$

for some  $\xi_i, \eta_j, x_i \leq \xi_i \leq x_{i+1}, y_{j-1} \leq \eta_j \leq y_{j+1}$ .

**Corollary 1.** If the exact solution  $\tilde{\mu}$  is slowly varying at  $x = 0$  and the initial condition is given by the direct inversion estimate  $\hat{\mu}$  [23, see theorem 3.2], then  $\exists \tilde{\alpha} > 0$  such that

$$|\tilde{\mu}_{i,j} - \tilde{\mu}_{i,j}| \leq \tilde{\alpha} + \hat{\alpha} (dx + dy),$$

where  $\tilde{\alpha} = 70 \exp(\alpha L) \frac{|\log \omega|}{\omega} \|\hat{\mu}_0\|_\infty \|\nabla \tilde{\mu}_0\|_\infty$ .

**Remark.** The exponential coefficients in the stability and accuracy results suggest that a extremely small step size  $dx_i$  may be needed to capture exponential growth stably and accurately. In the following section we present a method which both can perform better and has superior stability control.

#### 4. Log-elastographic nonlinear scheme

We now give the derivation and numerical analysis of the log-elastographic nonlinear scheme for solving the inverse problem model (8). Our method is inspired by Fattal and Kupferman [13], where their application is the simulation of viscoelastic flows. To get the nonlinear scheme, we start with a logarithmic variable transformation  $v = \log \tilde{\mu}$  by dividing both sides of (8) by  $\tilde{\mu}$  itself:

$$\begin{aligned} \tilde{\mu}_x + a(x, y)\tilde{\mu}_y + b(x, y)\tilde{\mu} + c(x, y) &= 0 \implies \\ \frac{1}{\tilde{\mu}}\tilde{\mu}_x + a(x, y)\frac{1}{\tilde{\mu}}\tilde{\mu}_y + b(x, y) + \frac{1}{\tilde{\mu}}c(x, y) &= 0 \implies \\ (\log \tilde{\mu})_x + a(x, y)(\log \tilde{\mu})_y + b(x, y) + c(x, y) \exp(-\log \tilde{\mu}) &= 0 \implies \\ v_x + a(x, y)v_y + b(x, y) + c(x, y)e^{-v} &= 0, \quad v = \log \tilde{\mu}. \end{aligned} \quad (13)$$

Then we can use the upwind finite difference formulation to discretize (13) based on the signs of  $a(x, y)$ :

$$\begin{aligned} \frac{v_{i+1,j} - v_{i,j}}{dx_i} + a_{i,j} \begin{cases} a_{i,j} \geq 0: & \frac{v_{i,j} - v_{i,j-1}}{dy} \\ a_{i,j} < 0: & \frac{v_{i,j+1} - v_{i,j}}{dy} \end{cases} + b_{i,j} + c_{i,j} e^{-v_{i,j}} &= 0 \implies \\ a_{i,j} \geq 0: & v_{i+1,j} = \left(1 - a_{i,j} \frac{dx_i}{dy}\right) v_{i,j} + a_{i,j} \frac{dx_i}{dy} v_{i,j-1} - (b_{i,j} + c_{i,j} e^{-v_{i,j}}) dx_i \\ a_{i,j} < 0: & v_{i+1,j} = \left(1 + a_{i,j} \frac{dx_i}{dy}\right) v_{i,j} - a_{i,j} \frac{dx_i}{dy} v_{i,j+1} - (b_{i,j} + c_{i,j} e^{-v_{i,j}}) dx_i. \end{aligned}$$

Taking the exponential on both sides of the finite difference formula, we get the nonlinear numerical scheme for  $\tilde{\mu}$ :

$$\begin{aligned} a_{i,j} \geq 0: & \tilde{\mu}_{i+1,j} = \tilde{\mu}_{i,j}^{(1-a_{i,j}dx_i/dy)} \tilde{\mu}_{i,j-1}^{a_{i,j}dx_i/dy} e^{-(b_{i,j} + \frac{c_{i,j}}{\tilde{\mu}_{i,j}})dx_i} \\ a_{i,j} < 0: & \tilde{\mu}_{i+1,j} = \tilde{\mu}_{i,j}^{(1+a_{i,j}dx_i/dy)} \tilde{\mu}_{i,j+1}^{-a_{i,j}dx_i/dy} e^{-(b_{i,j} + \frac{c_{i,j}}{\tilde{\mu}_{i,j}})dx_i} \\ 0 \leq i \leq m-1, & \quad 1 \leq j \leq n-1. \end{aligned} \quad (14)$$

Again, we consider two cases for the initial condition. First we assign the exact value as the initial condition and use the Neumann condition on the side boundaries. The stability result of this nonlinear scheme is given in the following lemma:

**Lemma 2.** Suppose  $dx_i$  is small enough such that  $|a_{i,j}|dx_i/dy \leq 1$  and the numerical solution satisfies  $\frac{\mu^*}{2} \leq \tilde{\mu} \leq 2\mu^{**}$  where the true solution satisfies  $\mu^* \leq \tilde{\mu} \leq \mu^{**}$ . Then  $\exists \beta = \max(-b_{i,j}) + \max 2(-c_{i,j})/\mu^*$  independent of step sizes such that

$$\|\tilde{\mu}_{i+1}\|_\infty \leq e^{\beta dx_i} \|\tilde{\mu}_i\|_\infty. \quad (15)$$

**Proof.** If we interpolate to make sure that  $|a_{i,j}|dx_i/dy \leq 1$ , then the sum of all the exponents of  $\tilde{\mu}$  on the right-hand side of (14) are non-negative. Assuming the exact solution is  $\tilde{\mu}$  and it is bounded as  $0 < \mu^* \leq \tilde{\mu} \leq \mu^{**}$ , we suppose the numerical solution  $\mu^*/2 \leq \tilde{\mu}_{i,j} \leq 2\mu^{**}$ ,

and then we can obtain the following result:

$$\begin{aligned} |\tilde{\mu}_{i+1,j}| &\leq e^{-(b_{i,j} + \frac{c_{i,j}}{\tilde{\mu}_{i,j}})dx_i} \max(|\tilde{\mu}_{i,j+1}|, |\tilde{\mu}_{i,j}|, |\tilde{\mu}_{i,j-1}|)^{[(1-\text{sign}(a_{i,j}))|a_{i,j}|\frac{dx_i}{dy}] + \text{sign}(a_{i,j})|a_{i,j}|\frac{dx_i}{dy}]} \\ &= e^{-(b_{i,j} + \frac{c_{i,j}}{\tilde{\mu}_{i,j}})dx_i} \max(|\tilde{\mu}_{i,j+1}|, |\tilde{\mu}_{i,j}|, |\tilde{\mu}_{i,j-1}|) \\ &\leq e^{\beta dx_i} \max(|\tilde{\mu}_{i,j+1}|, |\tilde{\mu}_{i,j}|, |\tilde{\mu}_{i,j-1}|), \quad \beta = \max_j(-b_{i,j}) + \frac{2}{\mu^*} \max_j(-c_{i,j}) \implies \\ \max_j |\tilde{\mu}_{i+1,j}| &\leq e^{\beta dx_i} \max_j |\tilde{\mu}_{i,j}| \implies \|\tilde{\mu}_{i+1}\|_\infty \leq e^{\beta dx_i} \|\tilde{\mu}_i\|_\infty, \end{aligned}$$

which proves the stability of the numerical scheme (14) in the infinity norm. □

**Theorem 2.** Suppose all assumptions from the previous lemma are satisfied and  $\tilde{\mu}_{i,j}$  is the exact solution of (8) at node  $(i, j)$ . If the initial condition is exact, then  $\exists \hat{\beta} > 0$  such that

$$\left| \frac{\tilde{\mu}_{i,j} - \tilde{\mu}_{i,j}}{\tilde{\mu}_{i,j}} \right| \leq \hat{\beta}(dx + dy),$$

where  $dx = \max_i dx_i$ .

**Remark.** The exact expression for  $\hat{\beta}$  in terms of the second derivatives of  $\log \tilde{\mu}$  and the bounds on  $\tilde{\mu}$  and  $\tilde{\mu}$  is given in the proof below.

**Proof.** Let us denote the difference between the exact solution and the numerical solution as  $er_{i,j} = \log \tilde{\mu}_{i,j} - \log \tilde{\mu}_{i,j} = \tilde{v}_{i,j} - v_{i,j}$ ; we will get

$$\frac{\tilde{v}_{i+1,j} - \tilde{v}_{i,j}}{dx_i} + a_{i,j} \begin{cases} a_{i,j} \geq 0 : & \frac{\tilde{v}_{i,j} - \tilde{v}_{i,j-1}}{dy} \\ a_{i,j} < 0 : & \frac{\tilde{v}_{i,j+1} - \tilde{v}_{i,j}}{dy} \end{cases} + b_{i,j} + c_{i,j} e^{-\tilde{v}_{i,j}} = \tau_{i,j},$$

where  $\tau_{i,j} = \frac{1}{2}\tilde{v}_{xx}(\xi_i, y_j) dx_i + \frac{1}{2}\tilde{v}_{yy}(x_i, \eta_j) dy$ ,  $x_i \leq \xi_i \leq x_{i+1}$ ,  $y_{j-1} \leq \eta_j \leq y_{j+1}$ .

Then we shall have

$$\begin{aligned} \begin{cases} a_{i,j} \geq 0 : & \tilde{v}_{i+1,j} = \left(1 - a_{i,j} \frac{dx_i}{dy}\right) \tilde{v}_{i,j} + a_{i,j} \frac{dx_i}{dy} \tilde{v}_{i,j-1} - (b_{i,j} + c_{i,j} e^{-\tilde{v}_{i,j}}) dx_i + \tau_{i,j} dx_i \\ a_{i,j} < 0 : & \tilde{v}_{i+1,j} = \left(1 + a_{i,j} \frac{dx_i}{dy}\right) \tilde{v}_{i,j} - a_{i,j} \frac{dx_i}{dy} \tilde{v}_{i,j+1} - (b_{i,j} + c_{i,j} e^{-\tilde{v}_{i,j}}) dx_i + \tau_{i,j} dx_i \end{cases} \implies \\ a_{i,j} \geq 0 : & er_{i+1,j} = \left(1 - \frac{a_{i,j} dx_i}{dy}\right) er_{i,j} + \frac{a_{i,j} dx_i}{dy} er_{i,j-1} + \frac{c_{i,j} dx_i}{\tilde{\mu}_{i,j}} (1 - e^{-er_{i,j}}) + \tau_{i,j} dx_i \\ a_{i,j} < 0 : & er_{i+1,j} = \left(1 + \frac{a_{i,j} dx_i}{dy}\right) er_{i,j} - \frac{a_{i,j} dx_i}{dy} er_{i,j+1} + \frac{c_{i,j} dx_i}{\tilde{\mu}_{i,j}} (1 - e^{-er_{i,j}}) + \tau_{i,j} dx_i. \end{aligned}$$

Now we consider the third term on the right-hand side of the finite difference formula of  $er_{i+1,j}$ :  $\frac{c_{i,j} dx_i}{\tilde{\mu}_{i,j}} (1 - e^{-er_{i,j}})$ . With the previous assumptions on the range of  $\tilde{\mu}$  and  $\tilde{\mu}$ , we get

$|er_{i,j}| = |\log \tilde{\mu}_{i,j} - \log \tilde{\mu}_{i,j}| \leq |\log \frac{\mu^*}{2\mu^{**}}|$ . We further conclude that

$$\begin{aligned} \text{if } er_{i,j} \geq 0 &\implies |1 - e^{-er_{i,j}}| \leq |er_{i,j}|, \\ \text{if } er_{i,j} < 0 &\implies |1 - e^{-er_{i,j}}| = e^{-er_{i,j}} - 1 \leq \frac{2\mu^{**} - 1}{\log \frac{2\mu^{**}}{\mu^*}} |er_{i,j}|. \end{aligned}$$

Then we have  $|1 - e^{-er_{i,j}}| \leq d|er_{i,j}|$ ,  $d = \max(1, (\frac{2\mu^{**}}{\mu^*} - 1)/\log \frac{2\mu^{**}}{\mu^*})$  and thus

$$\left| \frac{c_{i,j} dx_i}{\tilde{\mu}_{i,j}} (1 - e^{-er_{i,j}}) \right| \leq \frac{|c_{i,j}|d}{\mu^*/2} dx_i |er_{i,j}| \leq C dx_i |er_{i,j}|, \quad C = \frac{2d \max_{i,j} |c_{i,j}|}{\mu^*}.$$

And now with the previous stability requirement that  $|a_{i,j}|dx_i/dy \leq 1$ , we can show that:

$$|er_{i+1,j}| \leq \left(1 - \frac{a_{i,j} dx_i}{dy} + \frac{a_{i,j} dx_i}{dy}\right) \max(|er_{i,j-1}|, |er_{i,j}|, |er_{i,j+1}|) + C dx_i |er_{i,j}| + |\tau_{i,j}| dx_i \implies$$

$$\max_j |er_{i+1,j}| \leq (1 + C dx_i) \max_j |er_{i,j}| + dx_i \max_j |\tau_{i,j}| \implies$$

$$\begin{aligned} \|er_{i+1}\|_\infty &\leq e^{C dx_i} \|er_i\|_\infty + dx_i \|\tau_i\|_\infty \\ &\leq e^{C dx_i} e^{C dx_{i-1}} \|er_{i-1}\|_\infty + e^{C dx_i} dx_{i-1} \|\tau_{i-1}\|_\infty + dx_i \|\tau_i\|_\infty \\ &\leq e^{C dx_i} e^{C dx_{i-1}} e^{C dx_{i-2}} \|er_{i-2}\|_\infty + e^{C dx_i} e^{C dx_{i-1}} dx_{i-2} \|\tau_{i-2}\|_\infty \\ &\quad + e^{C dx_i} dx_{i-1} \|\tau_{i-1}\|_\infty + dx_i \|\tau_i\|_\infty \\ &\dots \\ &\leq \exp\left(C \sum_{k=0}^i dx_k\right) \|er_0\|_\infty + \sum_{k=0}^i \exp\left(C \sum_{l=0}^{i-k} dx_{l+k}\right) dx_k \|\tau_k\|_\infty. \end{aligned}$$

Since  $\exp(C \sum_{l=0}^{i-k} dx_{l+k}) \leq \exp(C \sum_{k=0}^i dx_k) = \exp(Cx_i)$ , we have

$$\begin{aligned} \|er_{i+1}\|_\infty &\leq \exp\left(C \sum_{k=0}^i dx_k\right) \|er_0\|_\infty + \sum_{k=0}^i \exp\left(C \sum_{l=0}^{i-k} dx_{l+k}\right) dx_k \|\tau_k\|_\infty \\ &\leq \exp(Cx_i) \|er_0\|_\infty + C^*(dx + dy) \exp(Cx_i)x_i, \end{aligned} \tag{16}$$

where  $dx = \max_{0 \leq k \leq i} (dx_k)$  and

$$C^* = \max_{0 \leq i \leq m} \left[ \max_{0 \leq j \leq n} \left( \frac{1}{2} \max(|\tilde{v}_{xx}(\xi_i, y_j)|, |\tilde{v}_{yy}(x_i, \eta_j)|) \right) \right]$$

is the upper bound of the constant involved in the ‘big O’ expression for the truncation error. Now we can assess the rate of the convergence of the nonlinear scheme (15) from (16):

$$\begin{aligned} \|er_{i+1}\|_\infty &= \max_j |er_{i+1,j}| \\ &= \max_j \left| \log \frac{\tilde{\mu}_{i+1,j}}{\tilde{\mu}_{i+1,j}} \right| \\ &\leq \exp(Cx_i) \|er_0\|_\infty + C^*(dx + dy) \exp(Cx_i)x_i. \end{aligned} \tag{17}$$

If the initial condition is exact, which means  $\|er_0\|_\infty = 0$ , we will get

$$\begin{aligned} \|er_{i+1}\|_\infty &= \max_j \left| \log \frac{\tilde{\mu}_{i+1,j}}{\tilde{\mu}_{i+1,j}} \right| \leq C^*(dx + dy) \exp(Cx_i)x_i \implies \\ \left| \frac{\tilde{\mu}_{i+1,j} - \tilde{\mu}_{i+1,j}}{\tilde{\mu}_{i+1,j}} \right| &\leq \max(1 - e^{-E(dx+dy)}, e^{E(dx+dy)} - 1) = e^{E(dx+dy)} - 1, \end{aligned}$$

where  $E = C^* \exp(Cx_i)x_i$ . Since  $\exp(E(dx+dy)) - 1 \leq E(dx+dy) \max(\exp(E(dx+dy))) = C^* \exp(Cx_i)x_i(dx+dy) \exp(C^* \exp(CL)L(dx+dy))$ , we have the estimate on the rate of convergence by denoting  $\hat{\beta} = C^* \exp(Cx_i)x_i \exp(C^* \exp(CL)L(dx+dy))$ :

$$\left| \frac{\tilde{\mu}_{i+1,j} - \tilde{\mu}_{i+1,j}}{\tilde{\mu}_{i+1,j}} \right| \leq \hat{\beta}(dx+dy). \tag{18}$$

As  $dx, dy \rightarrow 0$ , we pick  $x$  in the domain such that  $x_i \rightarrow x$  ( $i \rightarrow \infty$  as  $dx \rightarrow 0$ ) and thus

$$\begin{aligned} \left| \frac{\tilde{\mu}_{i+1,j} - \tilde{\mu}_{i+1,j}}{\tilde{\mu}_{i+1,j}} \right| &\leq \hat{\beta}(dx+dy) \\ &= C^* \exp(Cx_i)x_i \exp(C^* \exp(CL)L(dx+dy))(dx+dy) \\ &\rightarrow C^* e^{Cx} \exp(CL)L \cdot 0 = 0, \end{aligned}$$

which proves the first-order convergence of the nonlinear scheme. □

**Corollary 2.** *If the exact solution  $\tilde{\mu}$  is slowly varying at  $x = 0$  and the initial condition is given by the direct inversion estimate  $\hat{\mu}$  [23, see theorem 3.2], then  $\exists \tilde{\beta} > 0$  s.t.*

$$\left| \frac{\tilde{\mu}_{i+1,j} - \tilde{\mu}_{i+1,j}}{\tilde{\mu}_{i+1,j}} \right| \leq \tilde{\beta} + \hat{\beta}(\tilde{\beta} + 1)(dx+dy),$$

where  $\tilde{\beta} = \exp(\exp(CL) \left| \log(1 - 70 \frac{|\log \omega|}{\omega} \|\nabla \tilde{\mu}_0\|_\infty) \right|) - 1$  and also  $70 \frac{|\log \omega|}{\omega} \|\nabla \tilde{\mu}_0\|_\infty < 1$ .

- *Remark about the improved stability of the nonlinear scheme:* the nonlinear scheme introduced in this section has better control on the growth of the numerical solution than the semi-implicit upwind scheme, which can be easily demonstrated by comparing their stability results in areas where the exact shear modulus is constant. The forward problem model (1) reduces to the constant speed wave equation in those areas and the inverse problem model (8) effectively becomes

$$b(x, y)\tilde{\mu} + c(x, y) = 0, \tag{19}$$

which means that the numerical solution of the inverse problem satisfies  $b_{i,j}\tilde{\mu} + c_{i,j} = 0$  on every grid point. If we look at the stability result (15) of the nonlinear scheme without taking the infinity norm on both sides of inequality

$$|\tilde{\mu}_{i+1,j}| \leq e^{-(b_{i,j} + \frac{c_{i,j}}{\tilde{\mu}_{i,j}})dx_i} \max(|\tilde{\mu}_{i,j+1}|, |\tilde{\mu}_{i,j}|, |\tilde{\mu}_{i,j-1}|) \tag{20}$$

and apply the direct inversion solution as initial condition, it is obvious that the inequality (20) allows no growth of the numerical solution as the exponential term on the right-hand side is effectively equal to 1. On the other hand, the stability bound (12) of the upwind scheme without the infinity norm is

$$|\tilde{\mu}_{i+1,j}| \leq \frac{1}{1 + b_{i,j}dx_i} \max(|\tilde{\mu}_{i,j+1}|, |\tilde{\mu}_{i,j}|, |\tilde{\mu}_{i,j-1}|). \tag{21}$$

Even if the initial condition is exact, the inequality (21) still leaves room for the numerical solution to grow, which makes the numerical scheme less stable. The difference between the stability control of these two schemes is also highlighted in the case of rapidly changing shear modulus and this will be demonstrated later in the numerical reconstructions.

- *Remark about recovering multiple inclusions:* the semi-implicit upwind scheme and the log-elastographic nonlinear scheme only allow the information of the solution to propagate in one direction. This tends to give inaccurate results in cases where the solution contains strong backscattering along the  $x$ -axis. We introduce an elliptic scheme in the following section to utilize information propagating from all directions for model equation (9).

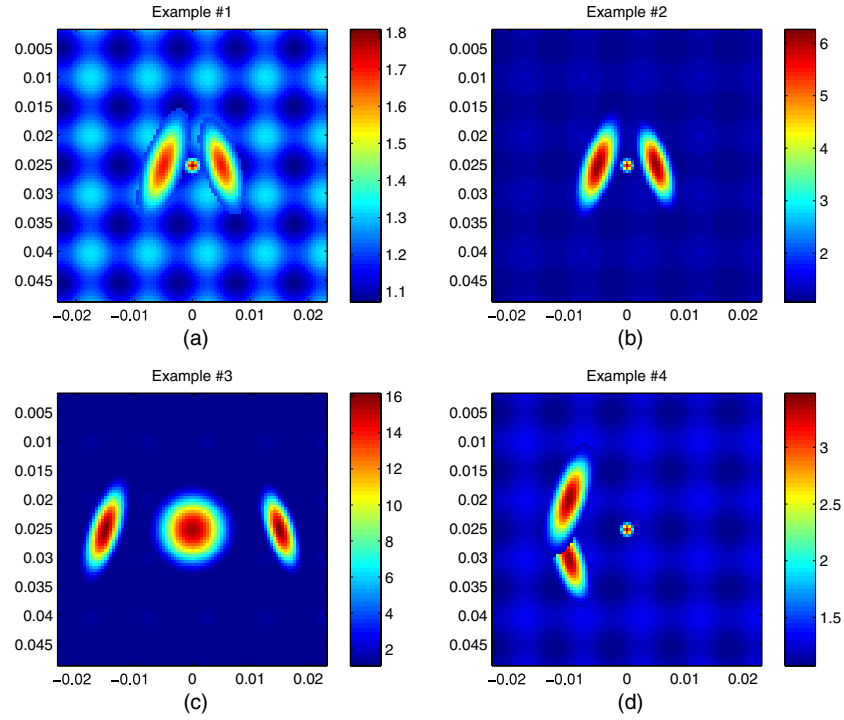


**Figure 1.** Exact value of four examples: (a) example 1, (b) example 2, (c) example 3 and (d) example 4.

## 5. Linear elliptic scheme

For the finite difference discretization of (9), the specific rule for choosing either upwind or downwind scheme is given below, it is guided by the goal of producing a diagonally dominant linear system:

*Case 1:*  $\Delta M_{i,j} - |\nabla \phi_{i,j}|^2 M_{i,j} < 0$ ,

$$M_{x,i,j} \frac{\frac{1}{2}(\text{sgn}(M_{x,i,j}) + 1)\tilde{\mu}_{i+1,j} - \text{sgn}(M_{x,i,j})\tilde{\mu}_{i,j} + \frac{1}{2}(\text{sgn}(M_{x,i,j}) - 1)\tilde{\mu}_{i-1,j}}{dx} + M_{y,i,j} \frac{\frac{1}{2}(\text{sgn}(M_{y,i,j}) + 1)\tilde{\mu}_{i,j+1} - \text{sgn}(M_{y,i,j})\tilde{\mu}_{i,j} + \frac{1}{2}(\text{sgn}(M_{y,i,j}) - 1)\tilde{\mu}_{i,j-1}}{dy} + \tilde{\mu}_{i,j}(\Delta M_{i,j} - |\nabla \phi_{i,j}|^2 M_{i,j}) + \omega_c^2 M_{i,j} = 0,$$

*Case 2:*  $\Delta M_{i,j} - |\nabla \phi_{i,j}|^2 M_{i,j} > 0$ ,

$$M_{x,i,j} \frac{-\frac{1}{2}(\text{sgn}(M_{x,i,j}) - 1)\tilde{\mu}_{i+1,j} + \text{sgn}(M_{x,i,j})\tilde{\mu}_{i,j} - \frac{1}{2}(\text{sgn}(M_{x,i,j}) + 1)\tilde{\mu}_{i-1,j}}{dx} + M_{y,i,j} \frac{-\frac{1}{2}(\text{sgn}(M_{y,i,j}) - 1)\tilde{\mu}_{i,j+1} + \text{sgn}(M_{y,i,j})\tilde{\mu}_{i,j} - \frac{1}{2}(\text{sgn}(M_{y,i,j}) + 1)\tilde{\mu}_{i,j-1}}{dy} + \tilde{\mu}_{i,j}(\Delta M_{i,j} - |\nabla \phi_{i,j}|^2 M_{i,j}) + \omega_c^2 M_{i,j} = 0,$$

where  $1 \leq i \leq m - 1$ ,  $1 \leq j \leq n - 1$ .

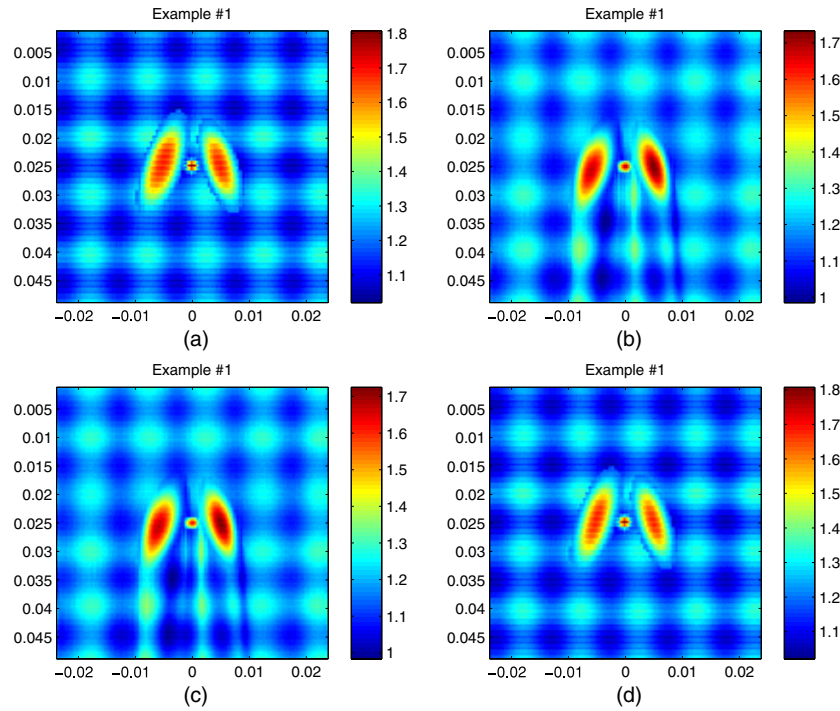


**Figure 2.** (a) Direct inversion recovery, (b) implicit upwind scheme recovery, (c) log-elastographic nonlinear scheme recovery and (d) elliptic scheme recovery.

The numerical scheme produces a sparse matrix system for  $\tilde{\mu}$ :

$$A\tilde{\mu} = b,$$

where  $b$  is composed of  $-\omega_c^2 M$  and the boundary data. The size of  $A$  is  $mn \times mn$  and the formulae for the elements of  $A$  is given by

$$A = (a_{k,l}), \quad 1 \leq k \leq mn, \quad 1 \leq l \leq mn,$$

$$a_{k,k} = \operatorname{sgn}(\Delta M_{i,j} - |\nabla \phi_{i,j}|^2 M_{i,j}) \left( \frac{|M_{x,i,j}|}{dx} + \frac{|M_{y,i,j}|}{dy} \right) + (\Delta M_{i,j} - |\nabla \phi_{i,j}|^2 M_{i,j}),$$

$$a_{k,k+1} = \frac{1}{2} [-\operatorname{sgn}(\Delta M_{i,j} - |\nabla \phi_{i,j}|^2 M_{i,j}) \operatorname{sgn}(M_{y,i,j}) + 1] \frac{M_{y,i,j}}{dy},$$

$$a_{k,k-1} = \frac{1}{2} [-\operatorname{sgn}(\Delta M_{i,j} - |\nabla \phi_{i,j}|^2 M_{i,j}) \operatorname{sgn}(M_{y,i,j}) - 1] \frac{M_{y,i,j}}{dy},$$

$$a_{k,k+n} = \frac{1}{2} [-\operatorname{sgn}(\Delta M_{i,j} - |\nabla \phi_{i,j}|^2 M_{i,j}) \operatorname{sgn}(M_{x,i,j}) + 1] \frac{M_{x,i,j}}{dx},$$

$$a_{k,k-n} = \frac{1}{2} [-\operatorname{sgn}(\Delta M_{i,j} - |\nabla \phi_{i,j}|^2 M_{i,j}) \operatorname{sgn}(M_{x,i,j}) - 1] \frac{M_{x,i,j}}{dx},$$

$$k = (i-1)n + j.$$

The structure of the matrix  $A$  makes sure that there are at most two off-diagonal elements at each row and the matrix is strictly row diagonally dominant as long as  $\Delta M_{i,j} - |\nabla \phi_{i,j}|^2 M_{i,j} \neq 0$ :

$$|a_{k,k}| = |\Delta M_{i,j} - |\nabla \phi_{i,j}|^2 M_{i,j}| + \frac{|M_{x,i,j}|}{dx} + \frac{|M_{y,i,j}|}{dy} > \sum_{l \neq k} |a_{k,l}| = \frac{|M_{x,i,j}|}{dx} + \frac{|M_{y,i,j}|}{dy}.$$

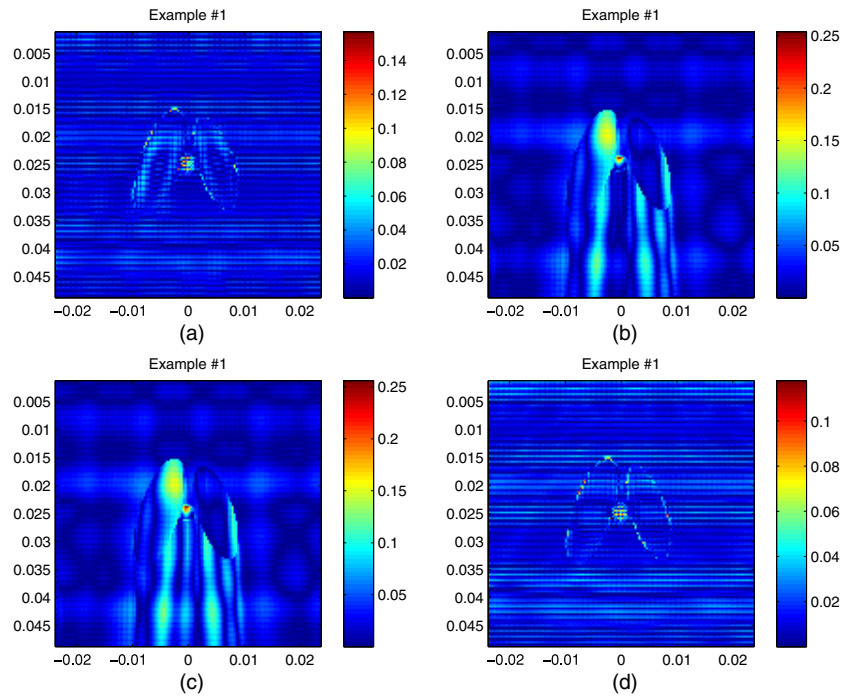


**Figure 3.** (a) Relative error of direct inversion recovery, (b) relative error of implicit upwind scheme recovery, (c) relative error of log-elastographic nonlinear scheme recovery and (d) relative error of elliptic scheme recovery.

The stability and accuracy of the matrix inversion is determined by the norm of  $A^{-1}$ . For this purpose, we first require Gerschgorin's theorem (1931) [39, p 71] as follows:

**Theorem 3.** Every eigenvalue of the matrix  $A$  lies in at least one of the circular discs with centers  $a_{k,k}$  and radii  $\sum_{l \neq k} |a_{k,l}|$ .

Then the accuracy result for the elliptic scheme can be established.

**Theorem 4.** If  $\Delta M - |\nabla \phi|^2 M$  is either negative or positive throughout the domain and exact Dirichlet boundary condition is applied, then the elliptic scheme is stable and convergent of first order.

**Proof.** Suppose  $\tilde{\mu}$  is the exact solution for equation (9). When we plug it into the elliptic scheme with the exact Dirichlet boundary conditions, we get

$$A\tilde{\mu} = b + \tau, \quad (22)$$

where  $\tau_k = \tau_{(i-1)n+j} = \frac{1}{2}\tilde{\mu}_{xx}(\xi_i, y_j) dx + \frac{1}{2}\tilde{\mu}_{yy}(x_i, \eta_j) dy$ , for some  $\xi_i, \eta_j, x_{i-1} \leq \xi_i \leq x_{i+1}, y_{j-1} \leq \eta_j \leq y_{j+1}$ . Suppose  $\tilde{\tilde{\mu}}$  is the numerical solution from the matrix system, then

$$A\tilde{\tilde{\mu}} = b. \quad (23)$$

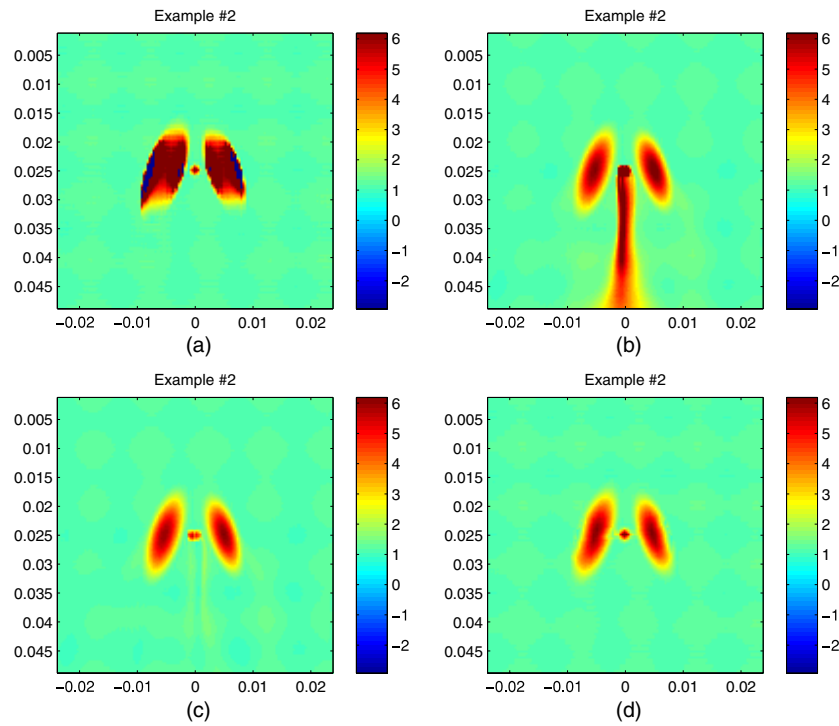


Figure 4. (a) Direct inversion recovery, (b) implicit upwind scheme recovery, (c) log-elastographic nonlinear scheme recovery and (d) elliptic scheme recovery.

Denote the error between the numerical solution and exact solution as  $e = \tilde{\mu} - \tilde{\tilde{\mu}}$ , then the difference between (23) and (22) gives

$$Ae = \tau. \tag{24}$$

Denote the eigenvalue of  $A$  with the smallest absolute value by  $\lambda_{\min}$ , then by Gerschgorin's theorem  $\exists 1 \leq p \leq n$  such that

$$|a_{p,p}| - |\lambda_{\min}| \leq |\lambda_{\min} - a_{p,p}| \leq \sum_{k \neq p} |a_{p,k}|.$$

From the formulae of all the entries of  $A$ , we get

$$|\lambda_{\min}| \geq |a_{p,p}| - \sum_{k \neq p} |a_{p,k}| = |\Delta M_{i_p, j_p} - |\nabla \phi_{i_p, j_p}|^2 M_{i_p, j_p}|.$$

Then as long as  $\Delta M - |\nabla \phi|^2 M$  is not changing sign and is continuous,  $|\lambda_{\min}|$  will be bounded below as  $dx, dy \rightarrow 0$  during the mesh refinement. This means that the biggest eigenvalue of  $A^{-1}$ , i.e.  $1/\lambda_{\min}$  is bounded above as  $dx, dy \rightarrow 0$  thus  $\|A^{-1}\|_{\infty}$  is bounded above by a constant  $C_{\lambda}$ . Hence

$$Ae = \tau \Rightarrow e = A^{-1}\tau \Rightarrow \|e\|_{\infty} \leq \|A^{-1}\|_{\infty} \|\tau\|_{\infty} \leq C(dx + dy) \rightarrow 0 \quad \text{as } dx, dy \rightarrow 0,$$

where  $C = C_{\lambda} \max_{i,j} \frac{1}{2} (|\tilde{\mu}_{xx}(\xi_i, y_j)|, |\tilde{\mu}_{yy}(x_i, \eta_j)|)$ . □

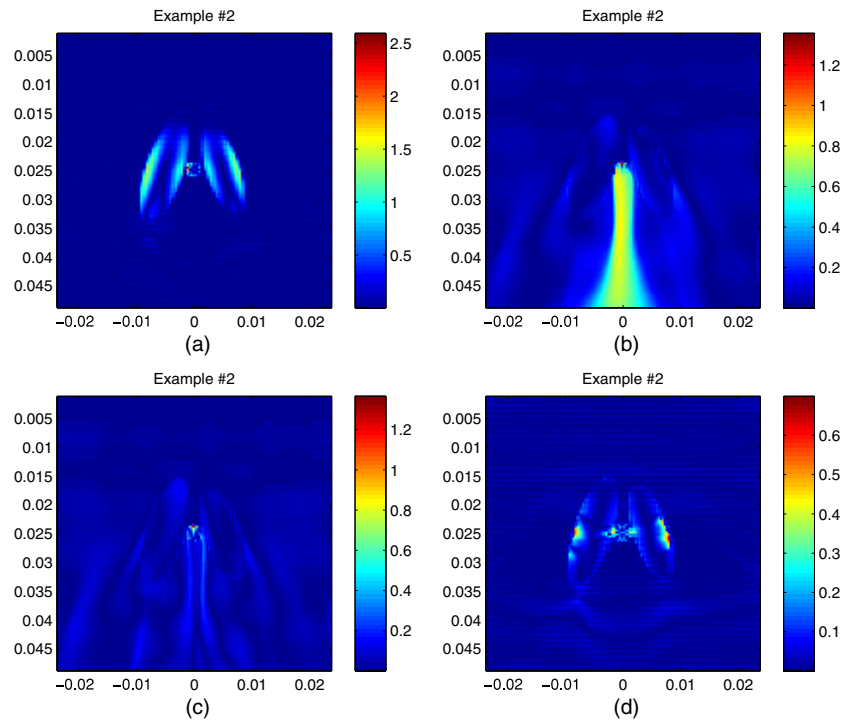


**Figure 5.** (a) Relative error of direct inversion recovery, (b) relative error of implicit upwind scheme recovery, (c) relative error of log-elasticographic nonlinear scheme recovery and (d) relative error of elliptic scheme recovery.

**Corollary 3.** *Suppose the Dirichlet boundary data is given by the direct inversion estimate and the exact solution is slowly varying around the boundary [23, see theorem 3.2], then  $\exists \hat{\tau} > 0$  such that*

$$\|e\|_\infty \leq C[(dx + dy) + \hat{\tau}],$$

where

$$\hat{\tau} = 70C \frac{|\log \omega|}{\omega} \|\tilde{\mu}_{i,j}\|_\infty \|\nabla \tilde{\mu}_{i,j}\|_\infty \frac{\max(\|M_{x,i,j}\|_\infty, \|M_{y,i,j}\|_\infty)}{\min(dx, dy)}$$

and the index  $(i, j)$  indicates that the norm is taken on boundary points  $(x_i, y_j) \in \partial\Omega$ .

*Remark on the implementation in complex geometries:* in many cases, the elliptic scheme can be easily implemented in complicated geometries provided that the grid in the region of interest is a subset of a rectangular grid. The matrix structure will change as well as the right-hand side. Essentially what occurs is that all points outside the region of interest and within a rectangular grid containing the complex geometry are set to zero. The associated rows and columns are eliminated. The direct inversion result is still utilized at all boundary points for the region of interest.

### 6. Numerical reconstructions from synthetic data

In this section, we test the semi-implicit upwind scheme, the log-elasticographic nonlinear scheme and the linear elliptic scheme with simulated data. We also compare their performances

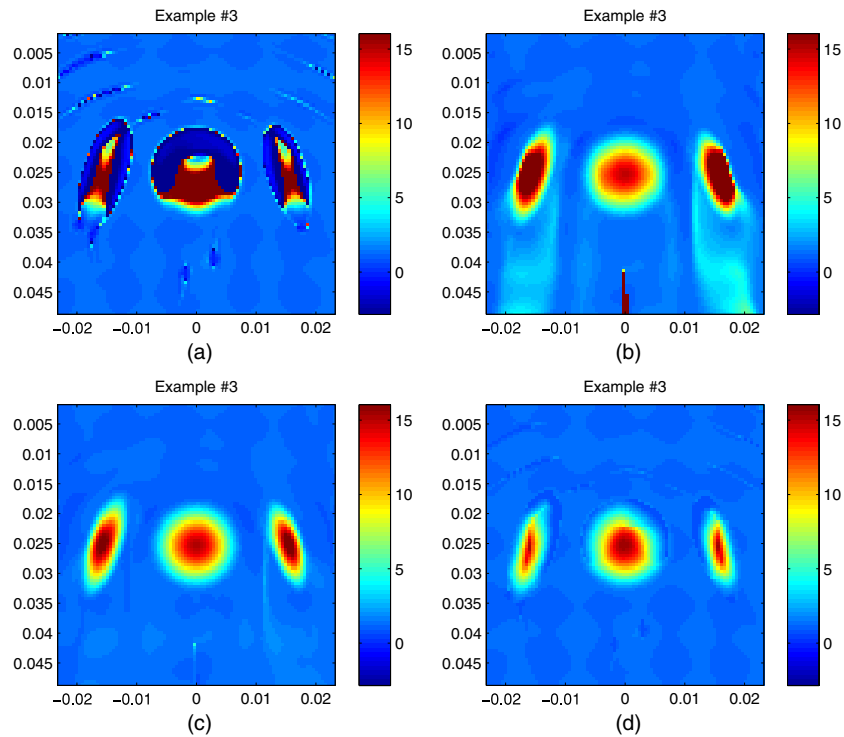


**Figure 6.** (a) Direct inversion recovery, (b) implicit upwind scheme recovery, (c) log-elastographic nonlinear scheme recovery and (d) elliptic scheme recovery.

with the performance of the direct inversion method previously investigated in [23]. The forward simulation is performed as given in [23]: we solve the acoustic wave equation

$$\nabla \cdot (\mu(x, y) \nabla u(x, y, t)) = \rho u_{tt}(x, y, t) \quad \text{in } \Omega \times (0, T)$$

with zero initial condition and with the Neumann boundary condition on top of the domain,  $x = 0$  where

$$\frac{\partial u}{\partial x}(y, 0, t) = \frac{1}{2\sqrt{\pi}c_t} \cos(\omega(t - t_0)) \exp\left[-\frac{(t - t_0)^2}{2c_t^2}\right].$$

The perfectly matched layer absorbing boundary condition (see [12, 23]) is implemented on the left, right and bottom of the domain. Here we choose  $t_0 = 0.05$ ,  $c_t = 0.01$  and  $\omega = 200\pi$ . To avoid an inverse crime, we use the synthetic data from the forward simulation to generate a new set of displacement data by a two-dimensional cubic spline interpolation instead of using the simulated data directly. The grid size of the new mesh is two-thirds of the grid size of the old mesh used in the forward simulation.

### 6.1. Performance test on data without noise

For data without noise, we Fourier transform the data set on the new mesh, extract the central frequency content and use eighth-order finite difference schemes to compute numerical derivatives to feed to the inversion schemes. We give four numerical examples here and their exact values are shown in figure 1. Each case has oscillatory shear modulus background defined by a 2D sinusoidal function with different sets of polynomial inclusions embedded.

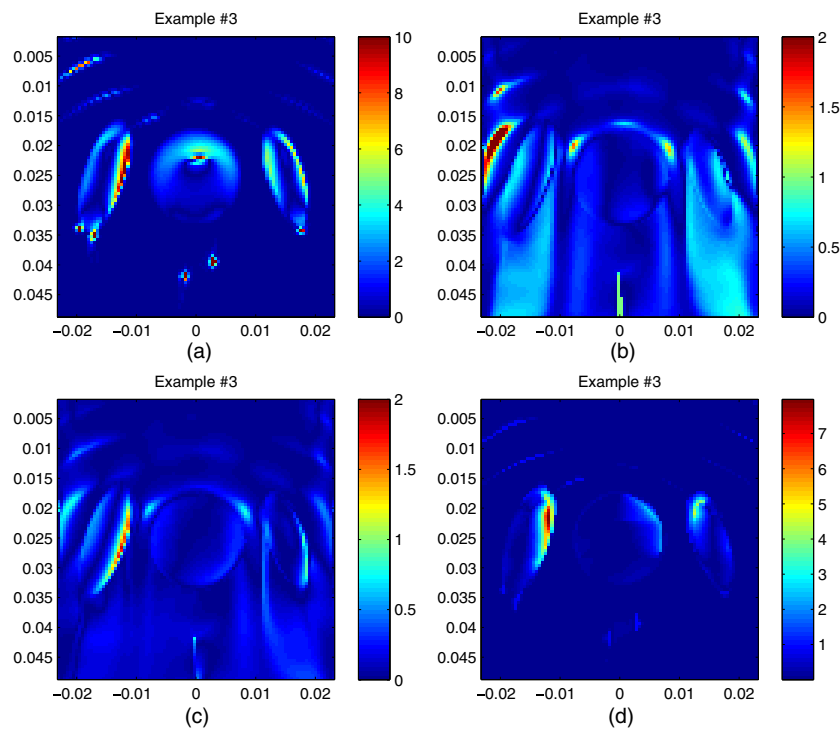


**Figure 7.** (a) Relative error of direct inversion recovery, (b) relative error of implicit upwind scheme recovery, (c) relative error of log-elastographic nonlinear scheme recovery and (d) relative error of elliptic scheme recovery. Notice that the ranges of the color bar vary.

The first example has two tilted ellipse inclusions and one small circular inclusion of radius 1.5 mm with relatively low amplitude. The numerical recoveries by all four methods are shown in figure 2 and the relative errors are shown in figure 3. In this case, all four methods give good reconstruction images while the direct inversion and the elliptic scheme perform best.

In the second example, we raise up the amplitude of all three inclusions from the first example to be 6 times higher than the background. The reconstructions are given in figure 4 and the relative differences are given in figure 5. Now the recovery of the direct inversion introduces negative values and thus fails the task. The semi-implicit upwind scheme handles the big inclusions well but produces a long artifact behind the small inclusion. In this case, the nonlinear scheme and the elliptic scheme give the best results.

Next we use an extreme example to demonstrate the stability of the nonlinear scheme. We now increase the radius of the circular inclusion to be 8 mm and raise the amplitude of all three inclusions to be about 16 times higher than the background. From the recoveries in figure 6 and the relative difference in figure 7, we can see that the direct inversion fails to recover the inclusions. All results are shown with amplitude up to the maximum of the exact value, thus the semi-implicit upwind scheme actually overshoots way above the correct value even though it recovers the location of the inclusions. The elliptic scheme has trouble at the front side of the inclusions while the nonlinear scheme gives the best result. This shows the superior control of the nonlinear scheme on the exponential growth of the solution. And the last two examples also confirm the relative error estimate introduced in [23].

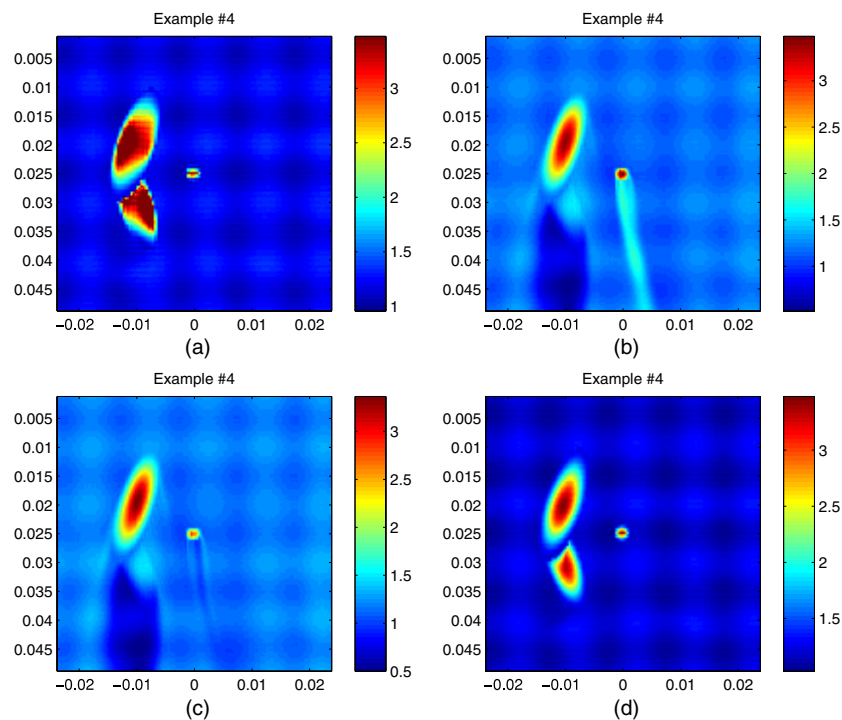


**Figure 8.** (a) Direct inversion recovery, (b) implicit upwind scheme recovery, (c) log-elastographic nonlinear scheme recovery and (d) elliptic scheme recovery.

The last case is where the performance of the elliptic scheme stands out. We move two tilted ellipse inclusions very close to each other and distribute them along the  $x$ -axis. Since the semi-implicit upwind scheme and the nonlinear scheme are marching from the top to the bottom of the domain, they fail to catch the peak of the second inclusion. In this case, the elliptic scheme recovers both peaks as it allows information to propagate in from all directions. The recoveries are given in figure 8 and the relative errors are given in figure 9.

- *Remark on well-spaced inclusions:* the last example is an extreme case to demonstrate the specific scenario when the hyperbolic schemes, like the implicit upwind scheme and the log-elastographic nonlinear scheme, cannot give satisfactory results. In general, however, the hyperbolic schemes and the elliptic scheme can all provide good recoveries when there is enough spacing between the inclusions along the wave propagation direction. The example given in figure 10 clearly shows that the hyperbolic schemes can recover the well-spaced inclusions very well.
- *Remark on numerical error from hyperbolic solvers:* the global hyperbolic solvers introduced in this paper, i.e. the implicit upwind scheme and the log-elastographic nonlinear scheme, are directional sweeping schemes where the vertical spatial dimension is treated as a pseudo time dimension. The numerical error generated at each time step is accumulated as the solvers march through the domain although this accumulated error has been proved to be convergent in previous sections when the step size goes to zero. In examples 1 and 2, the artifacts in the recoveries of the hyperbolic solvers behind the inclusions result from the effect of the accumulated numerical error on the recovery of

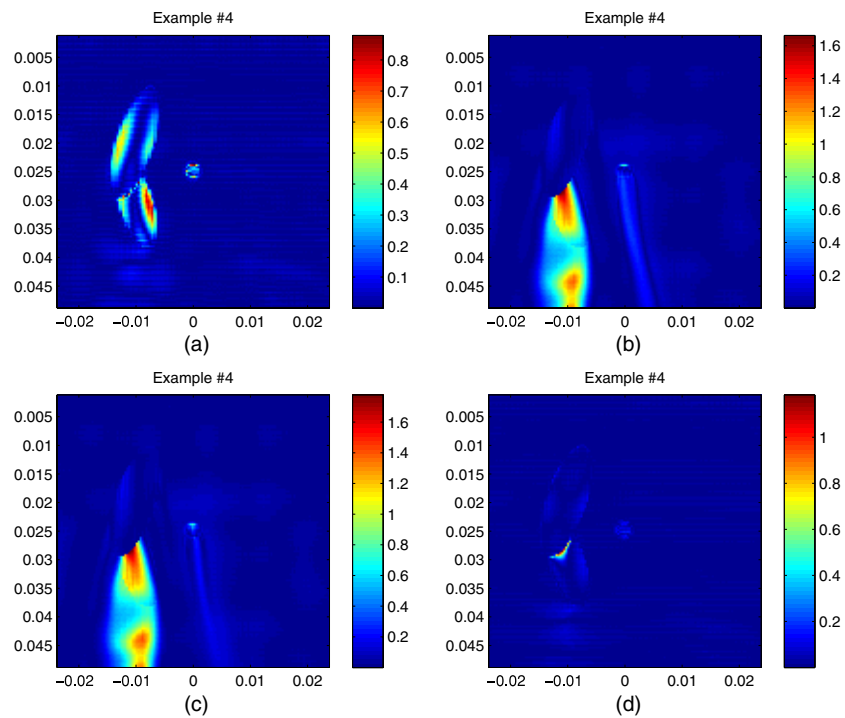


**Figure 9.** (a) Relative error of direct inversion recovery, (b) relative error of implicit upwind scheme recovery, (c) relative error of log-elastographic nonlinear scheme recovery and (d) relative error of elliptic scheme recovery.

the 2D sinusoidal oscillatory shear modulus background. In example 4, the presence of significant backscattering from the discontinuity of the shear modulus at the beginning of the second inclusion makes it difficult for the hyperbolic marching schemes to capture the inhomogeneity. The elliptic scheme allows information propagating from all directions and so the presence of strong backscattering has much less effect on the reconstructions.

- *Remark on the effect of initial and boundary conditions:* for all the 2D numerical examples, the initial conditions used in the hyperbolic schemes and the Dirichlet boundary conditions used in the elliptic scheme are the direct inversion recoveries. While our analysis of the hyperbolic schemes required a Neumann boundary condition, in our implementation we used a different approach. When the outflow condition is satisfied, we do not need boundary data and when the inflow condition is satisfied we use the direct inversion result. Since the exact shear modulus is either constant or slowly varying on the boundary of the domain, using the direct inversion results as initial and boundary conditions succeeds. This is consistent with the theoretical results established in previous sections (see corollaries 1–3). To further investigate the effect of direct inversion initial-boundary conditions, we test our inverse methods on two examples. In both cases, there are multiple polynomial inclusions. The 20 mm diameter circular inclusion is located on the boundary in the first case while in the second case it is moved inside the domain. The exact value of the shear modulus of these two examples are given in figure 11.

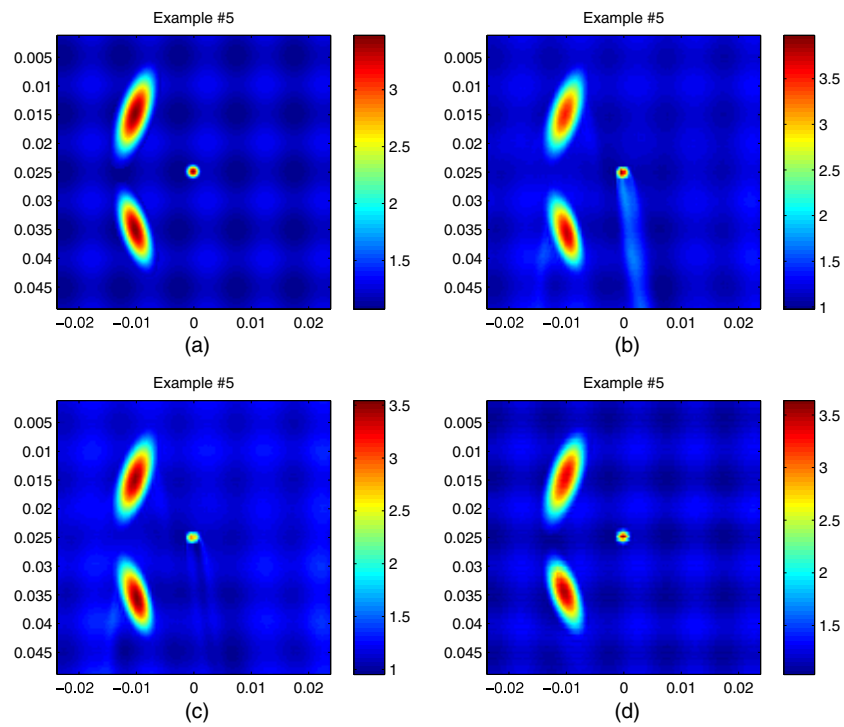


**Figure 10.** (a) Exact value, (b) implicit upwind scheme recovery, (c) log-elastographic nonlinear scheme recovery and (d) elliptic scheme recovery.

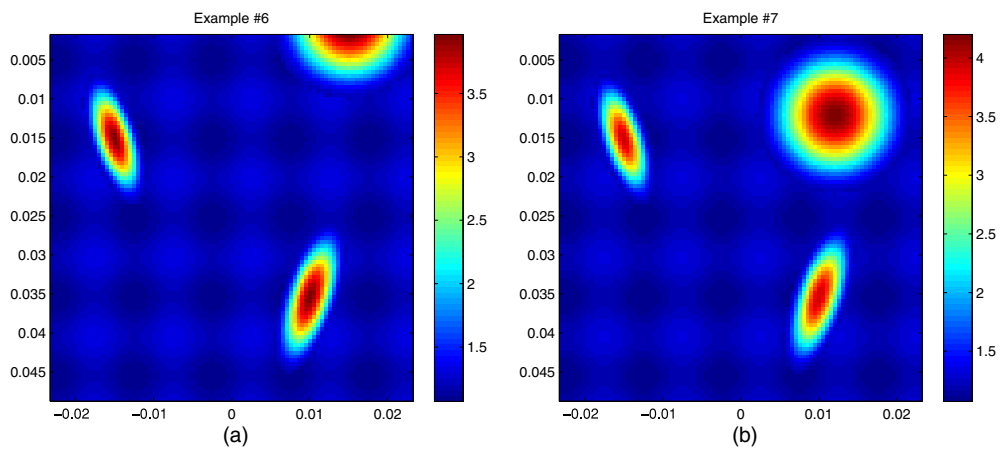


**Figure 11.** Exact value of shear modulus: (a) circular inclusion on the boundary and (b) circular inclusion inside the domain.

The reconstructions by all four inverse algorithms for the first case are presented in figure 12, while figure 13 gives the recoveries for the second case. From the numerical results, we can see that the error introduced by using the direct inversion recoveries as the initial condition and the boundary conditions does not have much effect on the hyperbolic

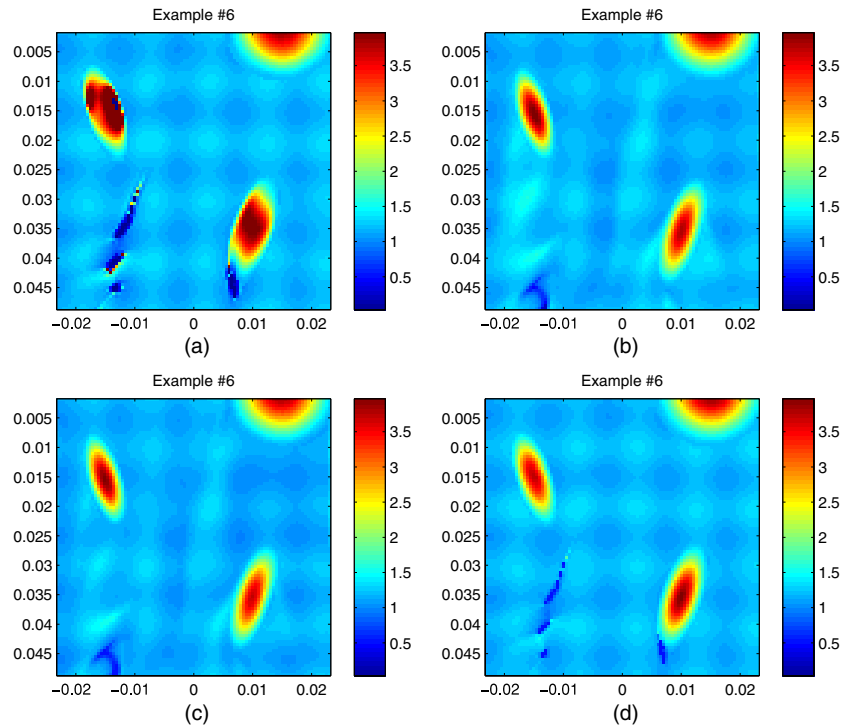


**Figure 12.** Example where there is boundary inclusion: (a) direct inversion recovery, (b) implicit upwind scheme recovery, (c) log-elastographic nonlinear scheme recovery and (d) elliptic scheme recovery.

solvers and the elliptic solver. The performance of the PDE solvers mainly depends on the stability and accuracy requirements.

### 6.2. Performance test on data with noise

While the numerical derivatives on clean synthetic data can be calculated accurately by high-order finite difference operators, it becomes a far more difficult issue when it comes to the same objective on noisy data. Simply applying finite difference operators will greatly amplify the numerical noise in the data and contaminate the results for numerical derivatives. In this section, we implement a statistically justified averaging scheme introduced by Anderssen and Hegland in [1] to perform numerical differentiation. This method ensures that the variance of the noise in the data is not amplified by the differentiation process and thus allows stable calculation of low-order derivatives from multi-dimensional noisy data. Here second-order central difference schemes are averaged in the scheme. The numerical example we give has oscillatory background and three inclusions, two ellipses and one circular disc. Figure 14 shows the exact shear modulus.

To test the stability of all four algorithms, we add Gaussian random noise to the interpolated displacement data on the new mesh:

$$u_{\text{noisy}}(x, y, t) = u(x, y, t) + \gamma u_{\text{max}} \text{randn}(x, y, t),$$

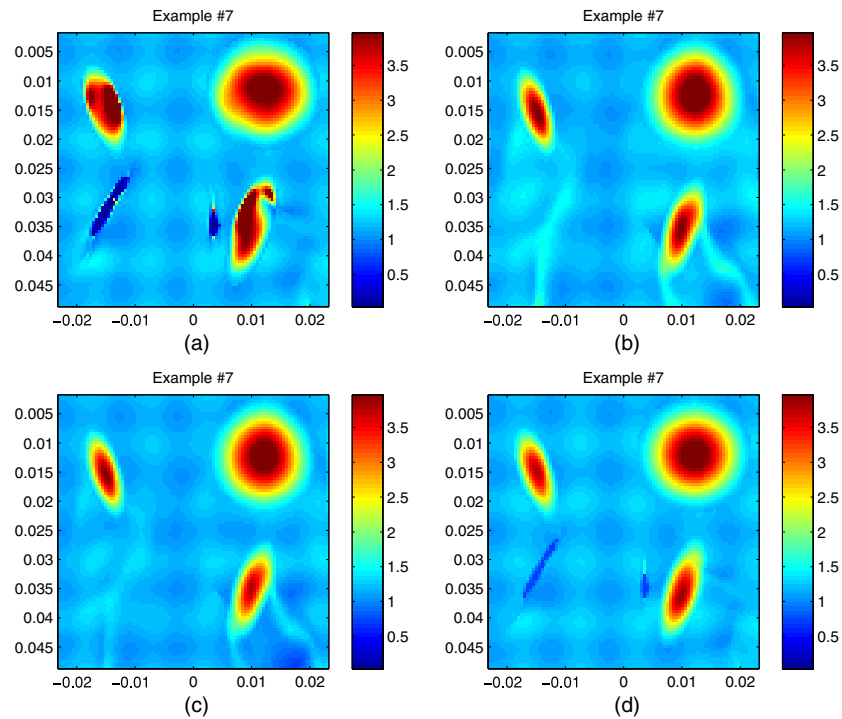


**Figure 13.** Example where boundary inclusion is moved inside: (a) direct inversion recovery, (b) implicit upwind scheme recovery, (c) log-elastographic nonlinear scheme recovery and (d) elliptic scheme recovery.

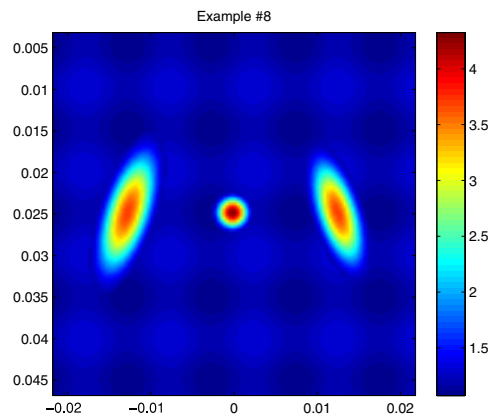


**Figure 14.** Exact value of shear modulus.

where  $u_{\max}$  is the maximum displacement,  $\gamma$  is the noise level and  $\text{randn}(x, y, t)$  is a random number generated in Matlab from the normal distribution with mean zero and variance one. For every numerical method, we Fourier transform the displacement to the frequency domain, pick four frequency frames, use the averaging method to compute numerical derivatives and

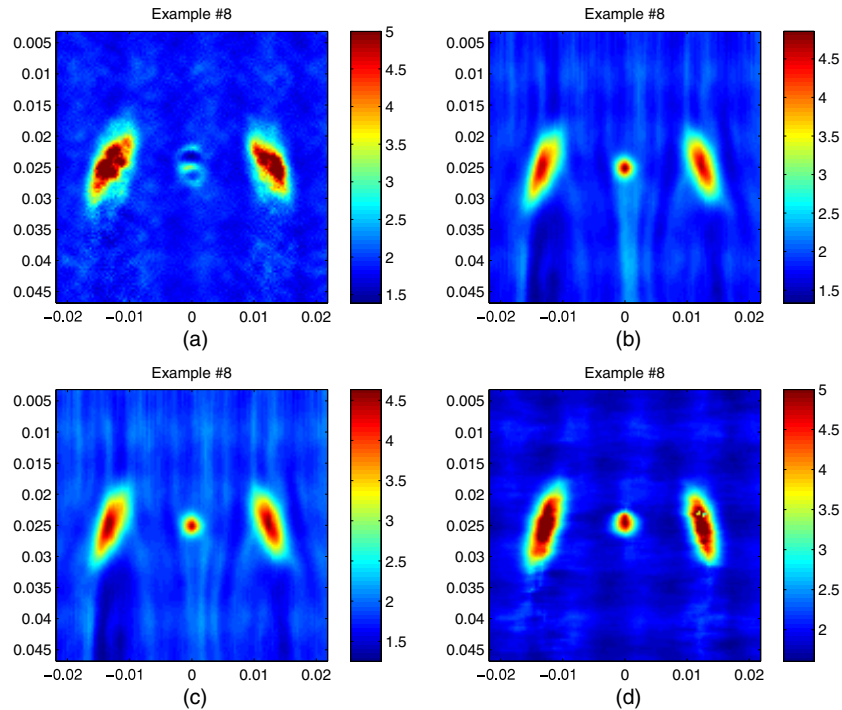


**Figure 15.** Recovery from noisy data with 10% Gaussian noise: (a) direct inversion recovery, (b) implicit upwind scheme recovery, (c) log-elastographic nonlinear scheme recovery and (d) elliptic scheme recovery.

get a recovery from each frame. The geometric mean of the four recoveries is then taken as the reconstruction result from that algorithm. Here, four frequency frames are used instead of one as an attempt to employ more information content. For our example we add 10% noise ( $\gamma = 0.1$ ) to the synthetic data. The results are given in figure 15 with no post-processing procedure to smooth out artifacts.

From the recoveries, we can see that all the methods tend to get good estimates of the location, shape and the amplitude of the two ellipse inclusions. However, the PDE solvers recover the small circular inclusion much better.

## 7. Conclusion and future work

We develop a log-elastographic nonlinear scheme and a finite difference based linear elliptic scheme for solving the first-order partial differential equation in the inverse problem of elastography. We show that both numerical schemes are stable and first-order accurate under certain assumptions. Compared with the implicit upwind scheme and the simple algebraic inversion scheme previously investigated (see [23]), the nonlinear scheme is more stable when the shear modulus is rapidly changing and the elliptic scheme has better performance in recovering complex structures in the shear modulus background. When the data are contaminated with Gaussian random noise, the PDE solvers tend to have better recoveries for small inclusions in the media.

## Acknowledgments

We have benefited from discussions with D Schwendeman, A Maniatty, A Oberai, P Zheglova. KL, JM and NZ were partially supported by ONR Grant No. N000 14-05-1-0600, ONR Grant No. N000 14-08-1-0432, NIBIB Grant No. 1R21EB003000-01 and NIA Grant No. R01AG029804.

## References

- [1] Anderssen R S and Hegland M 1999 For numerical differentiation, dimensionality can be a blessing! *Math. Comput.* **68** 1121–41
- [2] Bercoff J, Chaffai S, Tanter M, Sandrin L, Fink M, Gennisson J L and Meunier M 2003 In vivo breast tumor detection using transient elastography *Ultrasound Med. Biol.* **29** 1387–96
- [3] Bercoff J, Tanter M and Fink M 2004 Supersonic shear imaging: a new technique for soft tissue elasticity mapping *IEEE Trans. Ultrason. Ferroelectr. Freq. Control* **19** 396–409
- [4] Bercoff J, Muller M, Tanter M and Fink M 2001 Studying viscoelasticity in soft tissues with supersonic shear imaging *Acoust. Soc. Am. J.* **115** 2411–2
- [5] Bercoff J, Pernot M, Tanter M and Fink M 2004 Monitoring thermally-induced lesions with supersonic shear imaging *Ultrason. Imaging* **26** 71–84
- [6] Bercoff J, Tanter M, Chaffai S, Sandrin L and Fink M 2002 Ultrafast imaging of beamformed shear waves induced by acoustic radiation force: application to transient elastography *IEEE Ultrason. Symp. Proc.* vol 2 pp 1899–902
- [7] Bercoff J, Tanter M, Catheline S and Fink M 2001 Ultrafast compound imaging of 2D displacement vector measurements: application to transient elastography and color flow mapping *IEEE Ultrason. Symp. Proc.* vol 2 pp 1619–22
- [8] Catheline S, Bercoff J, Gennisson J L, Barriere C and Fink M 2004 Nonlinearity studies in soft tissues with the supersonic shear imaging system *IEEE Ultrason. Sympos.* **2** 1510–2
- [9] Catheline S, Gennisson J L, Delon G, Fink M, Sinkus R, Abouelkaram S and Culioli J 2004 Measurement of viscoelastic properties of homogeneous soft solid using transient elastography: an inverse problem approach *J. Acoust. Soc. Am.* **116** 3734–41
- [10] Catheline S, Thomas J-L, Wu F and Fink M 1999 Diffraction field of a low frequency vibrator in soft tissues using transient elastography *IEEE Trans. Ultrason. Ferroelectr. Freq. Control* **46** 1013–9
- [11] Ehman R L, Manduca A, McLaughlin J R, Renzi D and Yoon J-R 2006 Variance controlled shear stiffness images for MRE data *IEEE Int. Symp. Biomedical Imaging: Macro to Nano* 960–3
- [12] Francis C and Chrysooula T 2001 Application of the perfectly matched layer model to the linear elastodynamic problem in anisotropic heterogeneous media *Geophysics* **66** 294–307
- [13] Fattal R and Kupferman R 2005 Time-dependent simulation of viscoelastic flows at high Weissenberg number using the log-conformation representation *J. Non-Newton. Fluid Mech.* **126** 23–37
- [14] Fink M, Sandrin L, Tanter M, Catheline S, Chaffai S, Bercoff J and Gennisson J L 2002 Ultra high speed imaging of elasticity *IEEE Ultrason. Symp.* **2** 1811–20
- [15] Greenleaf J F, Muthupillai R, Rossman P J, Smith J, Manduca A and Ehman R L 1996 Direct visualization of strain waves by magnetic resonance elastography(MRE) 1996 *IEEE Ultrason. Symp. Proc.* vol 1 467–72
- [16] Gao L, Parker K J and Alam S K 1995 Sonoelasticity imaging: theory and experimental verification *J. Acoust. Soc. Am.* **97** 3875–80
- [17] Konofagou E E, Harrigan T and Ophir J 2000 Shear strain estimation and lesion mobility assesment in elastography *Ultrasonics* **38** 400–04
- [18] Knowles Ian 1999 Uniqueness for an elliptic inverse problem *SIAM J. Appl. Math.* **59** 1356–70
- [19] Konofagou E E 2000 Precision estimation and imaging of shear and normal components of 3D strain tensor in elastography *Phys. Med. Biol.* **45** 1553–63
- [20] Konofagou E E and Ophir J 1998 A new elastographic method for estimation and imaging of lateral displacements, lateral strains, corrected axial strains and Poisson's ratios in tissues *Ultrasound Med. Biol.* **24** 1183–99
- [21] Konofagou E E, Varghesse T and Ophir J 2000 Theoretical bounds on the estimation of transverse displacement, transverse strain and Poisson's ratios in elastography *Ultrasonic Imaging Ultrason. Imaging* **22** 153–77
- [22] Lin K 2008 Error estimation for the direct inversion model and numerical schemes for the full inversion model in elastography *PhD Thesis*
- [23] Lin K and McLaughlin J 2009 An error estimate on the direct inversion model in shear stiffness imaging *Inverse Problems* **25** 075003

- [24] Manduca A, Oliphant T E, Mahowald J L, Kruse S A, Amromin E, Felmlee J P, Greenleaf J F and Ehman R L 2001 Magnetic resonance elastography: non-invasive mapping of tissue elasticity *Med. Image Anal.* **5** 237–54
- [25] Oliphant T E, Kinnick R R, Manduca A, Ehman R L and Greenleaf J F 2000 An error analysis of Helmholtz inversion for incompressible shear, vibration elastography with application to filter-design for tissue characterization *IEEE Ultrason. Symp.* **2** 1795–8
- [26] Oliphant T E, Manduca A, Ehman R L and Greenleaf J F 2001 Complex-valued stiffness reconstruction for magnetic resonance elastography by algebraic inversion of the differential equation *Magn. Reson. Med.* **45** 299–310
- [27] Park E and Maniatty A 2006 Shear modulus reconstruction in dynamic elastography: time harmonic case *Phys. Med. Biol.* **51** 3696–721
- [28] Richter G 1981 An inverse problem for the steady state diffusion equation *SIAM J. Appl. Math.* **41** 210–21
- [29] Sinkus R, Siegmann K, Xydeas T, Tanter M, Clausen C and Fink M 2007 MR elastography of breast lesions: understanding the solid/liquid duality can improve the specificity of contrast-enhanced MR mammography *Magn. Reson. Med.* **58** 1135–44
- [30] Sandrin L, Tanter M, Catheline S and Fink M 2002 Shear modulus imaging with 2-D transient elastography *IEEE Trans. Ultrason. Ferroelectr. Freq. Control* **49** 426–35
- [31] Sandrin L, Tanter M, Gennisson J L, Catheline S and Fink M 2001 Shear elasticity probe in soft tissue with 1-D transient elastography *IEEE Trans. Ultrason. Ferroelectr. Freq. Control* **49** 436–46
- [32] Sinkus R, Tanter M, Xydeas T, Catheline S, Bercoff J and Fink M 2005 Viscoelastic shear properties of in vivo breast lesions measured by MR elastography *Magn. Reson. Imaging* **23** 159–65
- [33] Tanter M, Bercoff J, Sandrin L and Fink M 2002 Ultrafast compound imaging for 2D motion vector estimation: application to transient elastography *IEEE Trans. Ultrason. Ferroelectr. Freq. Control* **49** 1363–74
- [34] Taylor L S, Porter B C, Rubens D J and Parker K J 2000 Three-dimensional sonoelasticity: principles and practices *Phys. Med. Biol.* **45** 1477–94
- [35] Van Houten E, Doyley M, Kennedy F, Weaver J and Paulsen K 2003 Initial in vivo experience with steady-state subzone-based MR elastography of the human breast *J. Magn. Reson. Imaging* **17** 72–85
- [36] Van Houten E, Miga M, Weaver J, Kennedy F and Paulsen K 2001 Three-dimensional subzone-based reconstruction algorithm for MR elastography *Magn. Reson. Med.* **45** 827–37
- [37] Van Houten E, Paulsen K, Miga M, Kennedy F and Weaver J 1999 An overlapping subzone technique for MR-based elastic property reconstruction *Magn. Reson. Med.* **42** 779–86
- [38] Van Houten E, Weaver J, Miga M, Kennedy F and Paulsen K 2000 Elasticity reconstruction from experimental MR displacement data: initial experience with an overlapping subzone finite element inversion process *Med. Phys.* **27** 101–7
- [39] Wilkinson J H 1965 *The Algebraic Eigenvalue Problem* (Oxford: Oxford University Press)
- [40] Wu Z, Rubens D J and Parker K J 2006 Sonoelastographic imaging of interference patterns for estimation of shear velocity distribution in biomaterial *J. Acoust. Soc. Am.* **120** 535–45
- [41] Wu Z, Taylor L S, Rubens D J and Parker K J 2002 Shear wave focusing for three-dimensional sonoelastography *J. Acoust. Soc. Am.* **111** 439–46
- [42] Wu Z, Taylor L S, Rubens D J and Parker K J 2004 Sonoelastographic imaging of interference patterns for estimation of shear velocity of homogeneous biomaterials *Phys. Med. Biol.* **49** 911–22